BNL-108026-2015-JA

Long-term Measurements of Submicrometer Aerosol Chemistry at the Southern Great Plains (SGP) Using an Aerosol Chemical Speciation Monitor (ACSM)

Caroline Parworth[a], Jerome Fast[b], Fan Mei[b], Tim Shippert[b], Chitra Sivaraman[b], Alison Tilp[c], Thomas Watson[c], and Qi Zhang[a*]

[a] Department of Environmental Toxicology, University of California, 1 Shields Ave., Davis, California, USA 95616
[b] Pacific Northwest National Laboratory, Richland, Washington, USA 99354
[c] Brookhaven National Laboratory, Upton, New York, USA 11973

[*]Corresponding author: Qi Zhang
Department of Environmental Toxicology, University of California
1 Shields Avenue, Davis, California 95616
Phone: (530)-752-5779
Email: dkwzhang@ucdavis.edu

Accepted for publication in
Atmospheric Environment (January 2015)

Abstract

In this study the long-term trends of non-refractory submicrometer aerosol (NR-PM_1) composition and mass concentration measured by an Aerosol Chemical Speciation Monitor (ACSM) at the Atmospheric Radiation Measurements (ARM) program's Southern Great Plains (SGP) site are discussed. NR-PM_1 data was recorded at ~30 minute intervals over a period of 19 months between November 2010 and June 2012. Positive Matrix Factorization (PMF) was performed on the measured organic mass spectral matrix using a rolling window technique to derive factors associated with distinct sources, evolution processes, and physiochemical properties. The rolling window approach also allows us to capture the dynamic variations of the chemical properties in the organic aerosol (OA) factors over time. Three OA factors were obtained including two oxygenated OA (OOA) factors, differing in degrees of oxidation, and a biomass burning OA (BBOA) factor. Back trajectory analyses were performed to investigate possible sources of major NR-PM_1 species at the SGP site. Organics dominated NR-PM_1 mass concentration for the majority of the study with the exception of winter, when ammonium nitrate increases due to transport of precursor species from surrounding urban and agricultural areas and also due to cooler temperatures. Sulfate mass concentrations have little seasonal variation with mixed regional and local sources. In the spring BBOA emissions increase and are mainly associated with local fires. Isoprene and carbon monoxide emission rates were obtained by the Model of Emissions of Gases and Aerosols from Nature (MEGAN) and the 2011 U.S. National Emissions Inventory to represent the spatial distribution of biogenic and anthropogenic sources, respectively. The combined spatial distribution of isoprene emissions and air mass trajectories suggest that biogenic emissions from the southeast contribute to SOA formation at the SGP site during the summer.

Keywords: Aerodyne aerosol mass spectrometer (AMS); Rural; Organic aerosols; Back-trajectory analysis; Biomass burning

1. Introduction

Aerosols affect climate through scattering and absorption of radiation as well as influencing the overall radiative properties, precipitation efficiency, thickness, and lifetime of clouds. As described by the latest Intergovernmental Panel on Climate Change report (IPCC, 2014),

aerosols are one of the greatest sources of uncertainty in climate model predictions of radiative forcing. The U.S. Department of Energy's Atmospheric Radiation Measurement (ARM) program was established in 1990 to collect measurements needed to provide a better understanding and numerical representation of processes that affect atmospheric radiation in climate models (Stokes and Schwartz, 1994). Long-term continuous measurements have been collected at the Southern Great Plains (SGP) site near Lamont, Oklahoma since 1992; the Tropical Western Pacific (TWP) site on Manus Island in 1996; Nauru Island in 1998; Darwin, Australia in 2002; and the North Slope of Alaska (NSA) in Barrow, Alaska in 1997. The number and types of instruments deployed at these sites have evolved over time. Today, the SGP site is the most comprehensive climate research facility in the world with extensive in situ and remote sensing instrument clusters deployed over about 143,000 km^2. Most of the instruments at the SGP site measure radiation, cloud properties, and other meteorological quantities. Near-surface scattering and absorption by aerosols at multiple wavelengths is obtained from nephelometers and Particle Soot Absorption Photometers (PSAP), respectively (Sheridan et al., 2001), while the wavelength dependence of aerosol optical depth (τ) within the atmospheric column above the SGP site is obtained from sun photometers and MultiFilter Rotating Shadowband Radiometers (MFRSR) (Kassianov et al., 2005). Other important aerosol optical properties, such as single scattering albedo (ω_o), and asymmetry parameter, g, have been derived from the column MFRSR data.

Measurements of aerosol optical properties, such as τ, ω_o, and g are very useful for evaluating aerosol direct radiative forcing simulated by climate models. These quantities are also available worldwide from NASA's satellite and AErosol RObotic NETwork (AERONET) measurements (Dubovik et al., 2002; Holben et al., 1998) and have been used by many model evaluation and intercomparison studies, such as Aerosol Comparisons between Observations and Models (AeroCOM). The first AeroCOM intercomparison (Kinne et al., 2006) found that simulated τ was usually too low and that while the global averages were similar among the models there were relatively large differences in the regional distribution of τ. They also showed that there were large differences in simulated aerosol composition among the models. Myhre et al. (2013) subsequently showed that these and other differences in the climate model treatments contributed to a global mean aerosol direct radiative forcing that ranged from -0.58 to 0.02 W m^{-2}.

Fully understanding the sources of uncertainty contributing to this range of radiative forcing estimates requires additional evaluation of predicted aerosol mass, composition, and size distribution. While there have been few routine long-term measurements of these quantities worldwide, global climate models are now more frequently being evaluated with whatever in situ aerosol measurements are available. For example, Mann et al. (2014) recently evaluated the simulated aerosol size distribution with new observational data and showed that while the climate models qualitatively reproduced the observed mean size distributions, there were relatively large errors in certain regions and seasons and some models performed better than others. Spracklen et al. (2011) used a combined dataset of Aerosol Mass Spectrometer (AMS) observations to optimize secondary organic aerosol (SOA) sources in a global aerosol microphysics model – the Global Model of Aerosol Processes (GLOMAP) and verified the optimized SOA predictions against Interagency Monitoring of Protected Visual Environment (IMPROVE) network (Malm et al., 1994) measurements. Tsigaridis et al. (2014) focused on the performance of simulated organic aerosol (OA) among global models and found that increased complexity in the treatment of OA did not necessarily lead to improved results. In addition, the range of OA predictions widened in recent climate models compared to the previous AeroCOM intercomparison described by Kinne et al. (2006) because of the differences in the treatment of OA and the addition of highly uncertain OA precursor sources. One of these models, DOE's Community Atmosphere Model version 5 (CAM5), contains a more detailed treatment of the aerosol lifecycle than in the previous version (Liu et al., 2012), but simulated near surface OA was found to be too high when compared with IMPROVE network data over North America.

These studies demonstrate that co-located measurements of meteorology, radiation, and aerosols are needed to evaluate treatments of aerosol processes in climate models. Measurements characterizing chemical and physical properties of aerosols are important for understanding sources and processes of aerosols in the atmosphere, and can also be used to predict aerosol optical and hygroscopic properties. At the ARM SGP site, various instruments have been deployed over the years to measure aerosol size distribution, including most recently a Tandem Differential Mobility Analyzer (TDMA) and Aerosol Particle Sizer (APS). While daily filter samples of aerosols were collected between 2000 and 2008, more detailed and routine measurements of aerosol composition were not available until recently. An Aerosol Chemical Speciation Monitor (ACSM) (Ng et al., 2011b) has been deployed at the SGP Central Facility

since late 2010 to measure temporal variations in non-refractory submicron particulate matter (NR-PM_1) including OA, sulfate (SO_4^{2-}), nitrate (NO_3^-), ammonium (NH_4^+), and chloride (Cl^-). The ACSM is similar to the Aerosol Mass Spectrometer (AMS) that has been widely used to obtain aerosol composition measurements during field campaigns conducted throughout the world (Jimenez et al., 2009; Zhang et al., 2007a), except that it cannot measure particle size and is lower in cost, size, and weight. The lower cost of the ACSM also means lower sensitivity, thus less time resolution, when compared to the AMS, but the ACSM is better suited for long-term routine monitoring and thus provides information needed to evaluate the seasonal and yearly variability of aerosols simulated by climate models. For example, Sun et al. (2012) deployed an ACSM in Beijing, China to characterize organic and inorganic aerosols during the summer to understand high PM pollution events. Tiitta et al. (2014) describe the variation in aerosol composition measured by the ACSM over a one-year period in South Africa and quantify significant differences in aerosol mass and composition between the wet and dry seasons. In addition, Carbone et al. (2013) describe urban aerosol composition measured with the ACSM in Santiago de Chile over a period of three months.

In this study we analyze the ACSM measurements collected at the SGP site and quantify the diurnal, weekly, monthly, and seasonal variations in OA, sulfate, nitrate, ammonium, and chloride over 19 months. Positive Matrix Factorization (PMF) analysis of the organic mass spectra was performed using a 2-week rolling window algorithm to determine the OA factors and their variations over time. An analysis of back trajectories is used to illustrate potential sources of aerosols and aerosol precursors transported to the SGP site. The routine NR-PM_1 composition measurements at SGP will enable climate modelers to better identify the sources of uncertainties in aerosol radiative forcing simulations, when coupled to the existing extensive meteorological, radiation, aerosol optical property, and size distribution measurements. While there are routine aerosol composition measurements collected over the U.S. (e.g. IMPROVE network), they consist of averages over one-day or multi-day periods and those sites lack the detailed coincident measurements of radiation, aerosol optical properties, meteorology, and clouds needed to evaluate the factors contributing to aerosol radiative forcing. Compared to filter sampling, the ACSM will provide more detailed chemical speciation information with higher time resolution (< 1 hr) that can capture the dynamic variations of aerosol chemistry. Measurements of

atmospheric constituent at hourly or shorter time resolution are important for validating photochemical aerosol Chemical Transport Models (CTMs) (Wexler and Johnston, 2008).

2. Experimental Methods

2.1. SGP Site Description and ACSM Measurements

The location of the ACSM instrument deployed at the Central Facility of the ARM SGP site in north-central Oklahoma is shown in Figure S1 in the Supplementary Material. The land use in the vicinity of the Central Facility is rural and is composed of mixed farming (pasture, wheat, alfalfa, soybeans) and grassland. The nearest metropolitan areas are Wichita (population ~0.7 million) located ~110 km to the north, Oklahoma City (population ~1.3 million) located ~135 km to the south, and Tulsa (population ~1.1 million) located ~150 km to the southeast. Smaller cities such as Enid (population ~50,000), Stillwater (population ~47,000), and Ponca City (population ~25,000) are located 43 km to the south, 77 km to the southeast, and 42 km to the east of the Central Facility, respectively. ACSM measurements have been collected at ~30 min intervals since late 2010 and this analysis covers data from November 2010 through July 2012.

The ACSM sampled ambient air with a total flow rate of 3 L min^{-1}. The sample stream to the ACSM was dried with a Nafion dryer to avoid water condensation in the sampling line, which can influence collection efficiency (CE) of particles (Middlebrook et al., 2012). The ACSM measures the chemical composition of NR-PM_1. Detailed descriptions of the ACSM operating principles and calibration procedures are available elsewhere (Ng et al., 2011b). Briefly particles enter an aerodynamic lens through a critical orifice of 100 μm diameter at a rate of 0.1 L min^{-1} under vacuum. This focused particle beam impacts and vaporizes on a hot oven (~600°C), ionizes with 70eV electrons, and the resulting ions are detected using quadrupole mass spectrometry. Particle and background signals are differentiated using a 3-way valve automated switching system, which switches sample flow between ambient and particle-free air. More details on ACSM calibration and corrections can be found in the Supplementary Section 1.

2.2. Organic Aerosol Component Value-Added Product

Organic aerosols make up a large fraction of total NR-PM_1 mass (Zhang et al., 2007a) and can influence the radiative forcing of aerosols. Therefore it is important to study the chemical and physical properties of OA. The OA measured by the ACSM was investigated using the

Organic Aerosol Component (OACOMP) value-added product (VAP) (www.arm.gov/data/vaps). This VAP was developed to determine the sources and chemical evolution of OA from long term and continuously expanding ACSM datasets. The VAP can be described as a rolling window analysis that performs PMF (Paatero and Tapper, 1994) on long-term data in user-defined intervals. The procedure for the OACOMP VAP is discussed in detail in the Supplementary Section 2, and a brief explanation is given here. For this study PMF was performed on every 2 weeks of data, incrementing by 1 day, until the end of the data was reached. For every PMF analysis an OA ensemble mass spectral matrix and a measurement error matrix are calculated for a two-week period according to Ulbrich et al. (2009). Note that analysis of 2-weeks of data was chosen because this length captures the variations of aerosols and is representative of the average lifecycle of aerosols in the atmosphere (see Supplementary Section 2.1). Pretreatment is then applied to both matrices following the procedures given in Zhang et al. (2011). Specifically, problematic *m/z*'s (S/N< 0.2) were downweighted by a factor of 20 and weak *m/z*'s (0.2>S/N>2.0) were downweighted by a factor of 2. A minimum error of $1x10^{-2}$ μg m^{-3} was applied to the error matrix. Finally *m/z*'s 44, 18, 17, and 16 were downweighted by a factor of 2 because of the association of the latter 3 ions with *m/z* 44 in the organic fragmentation table. The PMF code is run on the two pretreated matrices to produce two to three factors using FPEAK = 0.0. The code allows for the possibility of 3 factors, including a BBOA factor and two types of OOA factors. No hydrocarbon-like factor is extractable in this dataset, which is consistent with the rural characteristics of the SGP site. A BBOA factor is identified if one factor has f_{60} (i.e., faction of total signal at *m/z* = 60) greater than or equal to 0.008. The two OOA factors are differentiated several ways, the first is based on f_{44} values, where the factor with greater f_{44} is identified as OOA-1 and the other as OOA-2. As factor profiles are produced OOA factors are also differentiated by comparing time series with previously adjacent time series in the rolling window analysis. Additional evidence to support the identification of each factor includes time series correlation with tracer species, diurnal variations in mass concentration, and characteristic mass spectral peaks. A more thorough description of the identification of factors is given in 3.2. The average time series can be found in the supplementary section (Fig. S3a-c) and the average mass spectrum of each factor obtained from the VAP are reported in Fig. 3a-c.

When used on long-term data the VAP results give insight into the variations of OA factors with respect to time of year and also quantify the uncertainties for each of the factors from PMF.

The main outputs of the VAP are mass spectra and mass concentration time series of OA factors that are representative of key sources, atmospheric formation and evolution processes, and physiochemical properties of OA (Zhang et al., 2011). Since the sum of all OA factors represents the total OA mass, these results are important for evaluating model predictions of sources and processes that contribute to total OA and also for closure studies on aerosol optical and cloud condensation properties. A better understanding of OA factors in the atmosphere from these results will also improve the representation of OA in models and help to reduce uncertainty associated with direct and indirect forcing of aerosols in climate models.

2.3. Back trajectory analyses

To illustrate the transport pathways and potential sources of aerosols observed at the SGP site, back trajectories were computed using the Hybrid Single-Particle Lagrangian Integrated Trajectory (HYSPLIT) model (Draxler and Rolph, 2013). Seven-day back trajectories were computed every three hours during the same time period as the ACSM measurements based on the large-scale meteorological fields available from the National Oceanic and Atmospheric Administration (NOAA) Global Data Assimilation System (GDAS). The horizontal spatial grid spacing of GDAS is 1 degree. All of the back trajectories originated 10 m above the ground at the SGP Central Facility and vertical transport was based on the mean vertical velocities from GDAS.

3. Results and Discussions

3.1. An overview of the variations in air mass trajectories

The seasonal variations in air mass transport to the SGP during 2011 based on HYSPLIT is shown in Figure 1 where the warmer colors denote higher frequently occurrence of back trajectory positions during each 3-month period. During the winter, northerly winds occur a larger fraction of time along with recirculating air masses over the south-central U.S. (Fig. 1a and 1e). Not surprisingly, transport to the SGP during the spring transition months is from both the south and north (Fig. 1b and 1f) that depends on position of high and low pressure systems passing through the region. Southerly winds dominate during the summer so that aerosols and their precursors are likely transported from Oklahoma and eastern Texas (Fig. 1c). The shorter back trajectories are due to wind speeds that are generally lower during the summer. The

transport pathways during the fall (Fig. 1d) were similar to those during the spring, except that there was less transport over southeastern Texas. This analysis also shows that air masses are unlikely to pass over the eastern and southwestern U.S. over the seven-day trajectory intervals. It is possible that air masses from the southeastern U.S. can be transported over the SGP site, but the transport period would be much longer than seven days. Note that back trajectories starting at higher altitudes where the wind speeds are higher would be longer than those shown in Figure 1; however, air masses would need to arrive over the SGP site at or below the top of the boundary layer.

The carbon monoxide (CO) emission rates from the 2011 National Emission Inventory and the emission rates for isoprene computed by the Model of Emissions of Gases and Aerosols from Nature (MEGAN) (Guenther et al., 2006) are shown in Figures 1g and 1h, respectively, for reference. The CO emissions represent the spatial distribution of anthropogenic sources, while the isoprene emissions represent the spatial distribution of biogenic sources. The isoprene emission rates are from a typical summer day, so the rates would be much lower during the winter. The high frequency of southerly winds suggests that Tulsa, Oklahoma City, and the Dallas-Fort Worth area likely contribute anthropogenic aerosol and aerosol precursors at the SGP site throughout the year. However these cities are 100 km or more from the SGP site so that dilution will reduce their concentrations before arriving at the SGP site. A large number of the trajectories pass during the summer over the high isoprene emissions regions east and southeast of the SGP site (Fig. 1c). This suggests that biogenic emissions likely contribute SOA mass at SGP primarily during the summer. Additional analysis relating observed biomass burning aerosol and inorganic aerosol species with the back trajectories is discussed in Section 3.4.

3.2. Temporal variations of submicron aerosol mass loading and composition

From November 20, 2010 to June 28, 2012 the temporal variations in meteorological conditions and NR-PM_1 particle composition and mass concentration at the SGP site are summarized in Figure 2.

The average ($\pm 1\sigma$) mass concentration of total NR-PM_1 over the entire dataset is 7.0 ($\pm$ 9.3) $\mu g\ m^{-3}$. A summary of the mass concentrations of major NR-PM_1 species for the entire study is shown in Table 1 and in Fig. S5. For the majority of the study, the molar equivalent ratios of ammonium to anions (i.e., nitrate, sulfate, and chloride) measured by the ACSM were calculated to be near 1, indicating that particles are fully neutralized and that inorganics are predominantly

in the forms of NH_4NO_3, $(NH_4)_2SO_4$, and NH_4Cl (Zhang et al., 2007b). As shown in Fig. 2c, the total NR-PM_1 mass concentration has a large range with substantially enhanced mass concentrations between February – May 2011 and February – March 2012. These spikes in NR-PM_1 are associated with increases in ammonium nitrate and the 2011 spikes are also associated with biomass burning emissions (Fig. 2d). This observation is consistent with the fact that prescribed agricultural burning in the region commonly occurs during spring months in preparation for crops (Reid et al., 2004).

Note that the time series of NR-PM_1 mass concentrations measured by the ACSM and PM_1 volume concentrations measured by a Tandem Differential Mobility Analyzer (TDMA) show similar trends (Fig. S4). However, the linear regression slope for comparing mass and volume measurements for the entire study period is ~2.7 g cm^{-3}, much higher than the average ($\pm 1\sigma$) density (ρ) of NR-PM_1 (1.40 ± 0.09 g cm^{-3}; Fig. 2b) estimated based on measured NR-PM_1 composition assuming that the densities of inorganics and organics are ~1.72 and ~1.2 g cm^{-3}, respectively. A possible reason for this discrepancy could be that different particle sizes are measured by the TDMA (12 – 712 nm) and ACSM (~ 30% transmission efficiency at 1 μm (Liu et al., 2007)). Comparisons of mass measured by the ACSM with filter measurements are not possible given that filter measurements at SGP were taken only for 2000-2007 and IMPROVE measurements do not cover the dates of this study. Furthermore we show seasonal differences in NR-PM_1 composition may be due to meteorological variations, thus comparing previous filter measurements with this dataset could be problematic.

From the VAP analysis of the OA dataset three factors were obtained including two types of OOA factors, where one is more oxidized with a higher f_{44} (i.e., faction of total signal at *m/z* = 44) than the other, and a biomass burning OA (BBOA) factor (Fig. 3). In order to test the overall performance of PMF, organic mass concentration was reconstructed from the three OA mass concentrations and correlated with the measured organic concentration from the ACSM (Fig. S6). From the linear regression it was determined that the approximated and measured organic mass are in good agreement with a linear regression slope of 1.004, intercept of 0.042, and r^2 = 0.987. The average mass spectra of the two OOA factors (Fig. 3a-b) show that f_{44} is higher for OOA-1 than OOA-2, and the fraction of total signal at *m/z* = 43 (f_{43}) is higher for OOA-2 than OOA-1. The ion signal at *m/z* = 44 commonly comes from the thermal decomposition of carboxylic acids on the vaporizer resulting in a CO_2^+ peak (Alfarra et al., 2004). The signal at

m/z = 43 mainly comes from the fragmentation of hydrocarbon chains to form $C_3H_7^+$ and carbonyls to form $C_2H_3O^+$. Therefore OOA-1 is representative of more-oxidized OA and OOA-2 is representative of less-oxidized OA. BBOA is a surrogate for OA emitted from biomass burning and has significant mass spectral peaks at *m/z* = 60 and 73, which are associated with anhydrous sugar such as levoglucosan emitted from wood burning (Alfarra et al., 2007; Schneider et al., 2006). BBOA mass concentration increases sporadically throughout the year but the majority of BBOA occurs during spring (41% of the days with BBOA influence) and winter (38%) and less frequently during summer (11%) and fall (9%). It is common to identify OOA types based on significant mass spectral peaks as well as mass concentration time series correlation with tracer species. In addition to having a large signal at *m/z* = 60, the BBOA factor also correlates well with the *m/z*=60 time series (Fig. S3c). Figure S7 shows the scatter plots of the OOA factors with secondary inorganic species colored by ambient temperature. OOA tends to have a temperature dependent correlation with nitrate such that the slope increases as temperature increases. Unlike nitrate, neither OOA factors nor sulfate concentrations are dramatically influenced by temperature (Fig. S8). The total OOA concentration correlates well with the sum of secondary inorganic (nitrate and sulfate) concentrations with similar temperature dependence discussed previously, thus supporting the secondary nature of OOA and the notion that OOA in this study likely consists of low-volatility species.

In Figure 4a is a triangle plot of organic f_{43} versus f_{44} for the entire dataset along with the range in f_{43} and f_{44} values for the three PMF factors obtained from the VAP analysis. The dotted lines represent the typical f_{43} and f_{44} bounds for OA factors found in previous global studies (Ng et al., 2010). Also shown in Fig. 4a and 4b are f_{44}, f_{43}, and f_{60} values from previous studies, including standard semi-volatile (SV-OOA) and low-volatility oxidized OA (LV-OOA) (Ng et al., 2011a); factors from Pasadena, CA (Hersey et al., 2011); Paris, FRA (Crippa et al., 2013); Zurich, CHE (Lanz et al., 2007); Fresno, CA (Ge et al., 2012b); and lab studies (http://cires.colorado.edu/jimenez-group/AMSsd/). OOA-1 is located near the apex of the triangle and is representative of highly aged and oxidized OA. OOA-2 is less oxidized than OOA-1 but is more oxidized than previously found SV-OOA factors that have lower f_{44} values. BBOA is the least oxidized OA of all the PMF factors found in this study. The box plots show the large range in oxidation for each OA factor and emphasize that constant factor profile mass spectra do not fully capture the dynamic variations of long-term datasets (more discussion in

Supplementary Section 3). Figure 4b shows that BBOA is within the range of f_{60} and f_{44} values found in previous ambient studies and the two OOA factors are distinct from the BBOA factor. Overall OA seems to be highly oxidized for most of the study such that the majority of data points are located near the apex of the triangle (OA have high f_{44} and low f_{43} values). An exception to this occurs during biomass burning events when f_{60} is high, OA is less oxidized, and elevated concentrations occur. This tendency for OA to be highly oxidized is consistent with the previous discussion that OOA consists mostly of low-volatility species.

3.3. Monthly, seasonal and diurnal variations of aerosol composition

It is difficult to see immediate trends in this long-term dataset and as a result it is useful to look at monthly, seasonal, and diurnal trends in aerosol composition and mass concentrations. Anthropogenic influences on NR-PM_1 chemistry were also investigated (see Supplementary Section 4). The major results from the 2011 dataset (Jan. – Dec. 2011) are summarized in Figure 5 to give insight into aerosol composition and concentration changes over the course of one year. This wheel plot shows how the NR-PM_1 composition, average concentration, OA composition, and wind change on a monthly basis. The largest average mass concentration in NR-PM_1 occurs between January – April due to a combination of lower atmospheric boundary layer (ABL) height, enhanced emissions of BBOA, and lower temperature that promotes the condensation of semi-volatile species such as ammonium nitrate and semi-volatile organic species (section 3.4). As ambient temperatures increase from May to August semi-volatile species decrease due to partitioning into the gas-phase. Overall the highest NR-PM_1 mass concentrations occur at the beginning of 2011 and decrease as the year progresses.

For the entire dataset (Nov. 2010 – June 2012) seasonal wind data and average mass concentrations and composition of NR-PM_1 are summarized in Figure 6. The highest NR-PM_1 mass concentration occurs in the winter of 2010-2011 and decreases from the spring to fall of 2011. Similar seasonal patterns are seen for 2012, such that beginning in the winter of 2011-2012 concentrations increase then decline in the following seasons. Therefore the cyclic nature of NR-PM_1 mass concentrations seen for 2011 (Fig. 5), where peak concentrations occur in the winter and decrease as the year progresses is also seen for the first half of 2012. The composition of NR-PM_1 is very similar among the same seasons, such that nitrate dominates NR-PM_1 mass concentration in both winters. All other seasons have organics contributing the most to total NR-PM_1 mass concentration. Changes in OA factor profiles with season were investigated for OOA-

1, OOA-2, and BBOA (Fig. S10) and more discussion can be found in the Supplementary Section 3.

The diurnal variations of major NR-PM_1 species concentration, temperature, and relative humidity separated by season are shown in Figures 7, S11, and S12. Most species lack distinct diurnal variations with the exception of nitrate. Aerosol nitrate is formed from the precursor gas HNO_3. The formation of HNO_3 can occur several ways including daytime reaction of NO_2 and OH radical and various nighttime reactions involving NO_3 radical and N_2O_5 (Seinfeld and Pandis, 2006). Two main diurnal patterns for nitrate are observed during this study that may be indicative of daytime and nighttime formation of HNO_3. Kim et al. (2014) have recently observed that daytime production of HNO_3 corresponds to a peak in total nitrate ($HNO_3 + NO_3^-$) production rate around late afternoon in the Northern US during winter. They also found that when nighttime production of HNO_3 is dominant, the total nitrate production rate peaks in the early morning and at night. Following this logic, at SGP during winter 2010-11 and spring 2011 the diurnal patterns of nitrate may be associated with nighttime production of HNO_3 whereas photochemical production of HNO_3 is likely responsible for the nitrate peaks in the mid-afternoon during fall 2011 and spring 2012. For the summer of 2011 nitrate concentrations are low and lack a strong diurnal variation. This diurnal pattern might be due to the abundance of nitrate in the form of organonitrates, which are less volatile and therefore less temperature dependent than more volatile species like ammonium nitrate (Perraud et al., 2012). Enhanced ratio of m/z = 30 to m/z = 46 provides evidence for organonitrates (Farmer et al., 2010). The average m/z 30:46 ratio for summer 2011 is ~10, substantially higher than the ratio for ammonium nitrate determined during ionization efficiency calibrations. This flat diurnal pattern for nitrate could also be related to competitive processes of nitrate production and evaporative loss during the daytime. Simultaneous measurements of nitric acid and ammonia would be needed to fully understand nitrate fluctuations. In addition to nitrate having a distinct diurnal pattern, BBOA in the spring shows enhanced concentrations during the early morning and throughout the evening, and suspected to be related to variability in ABL height.

With more than one year of data, the aerosol chemistry of overlapping seasons was compared, which for this dataset includes two winters (2010-11 and 2011-12) and two springs (2011 and 2012). The total NR-PM_1 concentration is greater for winter 2010-11 than winter 2011-12, mainly due to substantially higher concentrations of inorganic species, especially

nitrate (Fig. 6). The average concentrations of all aerosol species are much higher during spring 2011 than spring 2012 (Fig. 6), for which somewhat different source influences between the two years could be partly responsible. For example, according to the wind roses, the SGP site is subjected to more NW and NE winds in spring 2011 compared to spring 2012. Fire records also indicate that BB emissions during March 2012 are ~17% less than March 2011, and wind directions are not favorable to transport BB emissions to the site during March 2012 (Fig. S13).

In addition, winter 2010-11 and spring 2011 are overall colder and drier than winter 2011-12 and spring 2012, respectively (Fig. 7). Less influence of wet deposition might be a reason that both winter 2010-11 and spring 2011 have higher total NR-PM_1, whereas colder temperatures and more photochemical activities in winter 2011-12 and spring 2011 compared to the following winter and spring, respectively, might explain the higher fraction of nitrate in NR-PM_1 (Fig. 6). In addition, the fact that winter 2011-12 and spring 2012 have higher fractions of OOA-1 compared to winter 2010-11 and spring 2011 (Fig. 6) might be due to more humid conditions that facilitate aqueous phase processing (Ge et al., 2012a).

3.4. Sources of NR-PM_1

As shown in Figure 5, there is a substantial amount of BBOA present at the SGP site during February, March, and April of 2011. To better understand how smoke is transported to the SGP site, Figure 8 compares the temporal variations of BBOA with variations in fire locations and daily organic carbon (OC) emission rates from the Fire INventory from NCAR (Wiedinmyer et al., 2011) as well as back trajectories. As shown in Figure 8a, the high OC emissions within ~5 degrees (light gray shading) and ~2.5 degrees (dark gray shading) of the SGP site occur most frequently during March and April, corresponding to the highest overall monthly BBOA concentrations (Figures 5 and 8b). To examine the temporal variations in more detail, the daily OC emission rates and BBOA for March are shown in Figures 8c and 8d, respectively. Peak BBOA concentrations usually occur one to two days after high OC fire emissions. The exception is March 10-12 when BBOA is relatively low and fires with relatively higher emissions similar in magnitude to other events during the month occur southeast of the SGP site; however, most of the back trajectories show air masses at the SGP site on those days did not pass over those fires (not shown). As shown in Figure 8e, fires with the highest emission rates within 5 degrees of the SGP site occur in southeastern Oklahoma and western Arkansas, but the back trajectories (Figure 8g) suggest that a portion of the smoke during March could have originated from a large number

of smaller fires closer to the SGP site. In contrast, the number of fires during July 2011 was much less (Fig. 8f). While there were a few fires north of the SGP site, all of the back trajectories show transport from the south (Fig. 8h). The direction of those trajectories indicate that transport from the larger fires in the southeastern U.S. was possible, but the transport period was greater than 7 days so that any smoke originating from those fires are very dilute by the time they arrive at the SGP. The PMF approach is not able to identify very low concentrations of BBOA if they were present. In general, the BBOA at the SGP site is consistent with fire emission inventory and suggest that local fires contributed to the higher BBOA concentrations during the spring of 2011. Additional analyses using a chemical transport model would be needed to identify the relative contribution of each fire to the BBOA at the SGP site as well as to quantify the relative contribution of local and distant sources.

Figure 9 presents an analysis of temporal inorganic aerosol variations between January and March 2011 in relation to the spatial variations of ammonia, NO_x, and sulfur dioxide (SO_2) emissions and select back trajectories. Nitrate concentrations at SGP are highest during the winter months, with peak daily-averaged values exceeding 10 μg m^{-3} on 21 days between January and March 2011 (Fig. 9a), and multi-day variations in ammonium and nitrate are well correlated with each other. The coldest temperatures occur mostly in January and early February, with shorter periods of cold temperatures during March (Fig. 9b). It is evident that all of the high nitrate episodes are associated with temperatures below 3 ^{o}C (Fig. 9a). At warmer temperatures nitrate quickly partitions back to the gas phase, decreasing nitrate concentrations. The sources of nitrogen from surface ammonia and NO_x emissions are shown in Figures 9c and 9d, respectively. A significant amount of NO_x is also emitted from numerous power plants (not shown). Relatively low emission rates of both NH_3 and NO_x occur in the immediate vicinity of the SGP site and higher emission rates are located several hundred kilometers or more away. The back trajectories associated with nitrate > 10 μg m^{-3} (Fig. 9e) pass over different ammonia and NO_x emission sources in all directions prior to arriving at the SGP site. A similar analysis of the back trajectories associated with nitrate > 3 μg m^{-3} for January, February, and March are shown in Figures 9f, 9g, and 9h, respectively. During January when the temperatures are the coldest overall, back trajectories are primarily from the north to northwest and pass over the relatively higher ammonia emissions in Nebraska (Fig. 9f). During February (Fig. 9g), the transport pathways are similar to January except there are a few days in which transport is from the south

446 suggesting that NO_x sources from Oklahoma City and Dallas-Fort Worth may have contributed
447 to nitrate. Transport from the south becomes more frequent during early spring in March (Fig.
448 9h). Thus, the relative contribution of ammonia and NO_x on nitrate likely depends on the
449 ambient winds and the emission rates upwind are sufficiently high to produce nitrate
450 concentrations as long as the temperature is sufficiently low.
451 In contrast with other rural areas of the world (Zhang et al., 2011) (e.g., sulfate accounts for
452 an average ~39% of total NR-PM_1 concentration), sulfate at the SGP site is a relatively lower
453 fraction of the total aerosol concentrations. As shown in Figure 2d, sulfate concentrations exceed
454 2 μg m^{-3} on 82 days between January and June, but concentrations are much lower for the
455 remainder of the year. Nevertheless, the fraction of sulfate to the total aerosol concentration
456 changes little during the year (Fig. 6). Temporal variations in sulfate for January through March
457 are shown in Figure 9i in relation to the variations of nitrate and ammonium. Sulfate is not
458 correlated with temperature because of its longer lifetime (Fig. S7). There are numerous point
459 sources of sulfur dioxide (SO_2) surrounding the SGP site with many small emission sources (<
460 10^{-5} ton day^{-1}) and fewer locations where emissions exceed 0.1 ton day^{-1} (Fig. 9j – 9l). Area
461 sources of sulfur dioxide are not shown since they are much smaller than the point sources.
462 During January (Fig. 9j), the peaks in sulfate concentrations are likely from three large sulfur
463 dioxide emission sources close to the SGP site, one located a few kilometers southwest of the
464 SGP site, one in south-central Kansas, and the other close to Oklahoma City. During February
465 (Fig. 9k), the trajectories indicate a more broad distribution of SO_2 sources located southwest,
466 south, and southeast of the SGP site in Oklahoma contribute to peak sulfate concentrations. In
467 contrast, peak sulfate concentrations are mostly associated with transport by northeasterly winds
468 from SO_2 sources in southeastern Kansas during March (Fig. 9l). There are still a few periods in
469 which transport is from other directions. The locations of the SO_2 sources and the variable winds
470 at the SGP site suggest that many sources can contribute to sulfate at the SGP site. The closest
471 SO_2 sources with the highest emission rates may not be the biggest contributors to the overall
472 sulfate concentrations during much of the year. The higher sulfate concentrations during the
473 winter months are also due to lower boundary layer depths that inhibit vertical mixing. This
474 simple analysis cannot point to the role of aqueous chemistry in clouds that could enhance
475 sulfate over transport periods of many days.

While the back trajectories provide some insight into the transport pathways associated with changes in aerosol composition, questions regarding the aerosol precursor sources and mechanisms contributing to the observed multi-day and seasonal variations in aerosol composition are best addressed by regional chemical model studies. The data set also provides a useful metric to evaluate global model predictions of aerosol composition.

4. Summary and Conclusions

In this study the long-term seasonal, diurnal, weekly, and monthly trends for NR-PM_1 mass concentration and composition are summarized for the SGP site. High mass concentration periods of NR-PM_1 occur predominantly in the spring and winter months, due to increased emissions of BBOA and formation of ammonium nitrate, respectively. Back trajectory analyses show that BBOA during the spring is mainly from local burning emissions. Cooler ambient temperatures that favor gas-to-particle partitioning and long-range transport of NO_x and ammonia from urban and agricultural areas, respectively, resulted in elevated concentrations of ammonium nitrate during the winter. There are no significant seasonal trends in sulfate concentrations and a mixture of local and regional sources are expected for sulfate. An OACOMP VAP was developed allowing PMF to be performed on long term ACSM data using a rolling window technique, which captures the dynamic variations of chemical composition and concentration in the OA components over time. For the first time PMF analysis using the OACOMP VAP was performed to determine distinct OA factors, which consist of BBOA and two types of OOA, differing in degrees of oxidation. For most of the study organics are aged and highly oxidized, with the exception to this occurring during biomass burning events. The rolling-window PMF results uniquely capture the dynamic variations of atmospheric oxidation and age for each of the PMF factors.

Long-term and high time resolution aerosol mass and composition measurements from this study can be combined with meteorological, radiation, aerosol optical property, and size distribution measurements from SGP to evaluate aerosol radiative forcing simulations. As this dataset continues to expand, it will be useful for observing changes in aerosol composition and concentration over multiple years. The aerosol composition data can also be coupled with other ARM SGP measurements of meteorology, radiation, and aerosol optical and hygroscopic

505 properties to evaluate how well climate models represent the seasonal and multi-year variations
506 in aerosol radiative forcing at this site.

507 Acknowledgments

508 This research was supported by the US Department of Energy (DOE), the Office of Science
509 (BER), Atmospheric System Research Program, grant No. DE-FG02-11ER65293 and the
510 National Science Foundation (NSF) Graduate Research Fellowship under grant No. DGE-
511 1148897. Data from the SGP site was supported by the DOE Atmospheric Radiation
512 Measurement (ARM) program. The authors gratefully acknowledge the NOAA Air Resources
513 Laboratory (ARL) for the provision of the HYSPLIT transport and dispersion model and/or
514 READY website (http://www.ready.noaa.gov) used in this publication. PNNL is operated for the
515 US DOE by Battelle Memorial Institute under contract DE-AC05-76RL01830.

516

References

Alfarra, M.R., et al., 2004. Characterization of urban and rural organic particulate in the lower Fraser valley using two aerodyne aerosol mass spectrometers. Atmos. Environ. 38, 5745-5758.

Alfarra, M.R., et al., 2007. Identification of the mass spectral signature of organic aerosols from wood burning emissions Environ. Sci. and Technol. 41, 5770-5777.

Carbone, S., et al., 2013. Chemical Characterization of Submicron Aerosol Particles in Santiago de Chile. Aerosol and Air Quality Research 13, 462-473.

Crippa, M., et al., 2013. Wintertime aerosol chemical composition and source apportionment of the organic fraction in the metropolitan area of Paris. Atmos. Chem. Phys. 13, 961-981.

Cubison, M.J., et al., 2011. Effects of aging on organic aerosol from open biomass burning smoke in aircraft and laboratory studies. Atmos. Chem. Phys. 11, 12049-12064.

Draxler, R.R., Rolph, G.D., 2013. HYSPLIT (HYbrid Single-Particle Lagrangian Integrated Trajectory) Model access via NOAA ARL READY Website NOAA Air Resources Laboratory, College Park, MD.

Dubovik, O., et al., 2002. Variability of absorption and optical properties of key aerosol types observed in worldwide locations. Journal of the Atmospheric Sciences 59, 590-608.

Farmer, D.K., et al., 2010. Response of an aerosol mass spectrometer to organonitrates and organosulfates and implications for atmospheric chemistry. Proceedings of the National Academy of Sciences of the United States of America 107, 6670-6675.

Ge, X., et al., 2012a. Effect of Aqueous-Phase Processing on Aerosol Chemistry and Size Distribution in Fresno, California, during Wintertime. Environmental Chemistry 9, 221-235.

Ge, X.L., et al., 2012b. Primary and secondary organic aerosols in Fresno, California during wintertime: Results from high resolution aerosol mass spectrometry. J. Geophys. Res.-Atmos. 117.

Guenther, A., et al., 2006. Estimates of global terrestrial isoprene emissions using MEGAN (Model of Emissions of Gases and Aerosols from Nature). Atmos. Chem. Phys. 6, 3181-3210.

Hersey, S.P., et al., 2011. The Pasadena Aerosol Characterization Observatory (PACO): chemical and physical analysis of the Western Los Angeles basin aerosol. Atmos. Chem. Phys. 11, 7417-7443.

Holben, B.N., et al., 1998. AERONET - A federated instrument network and data archive for aerosol characterization. Remote Sensing of Environment 66, 1-16.

IPCC, 2014. IPCC: Climate Change 2013 – The Physical Basis, 2014: Working Group I Contribution to the Fifth Assessment Report to the Intergovernmental Panel on Climate Change (IPCC).

Jimenez, J.L., et al., 2009. Evolution of Organic Aerosols in the Atmosphere. Science 326, 1525-1529.

Kassianov, E.I., et al., 2005. Retrieval of aerosol microphysical properties using surface MultiFilter Rotating Shadowband Radiometer (MFRSR) data: Modeling and observations. J. Geophys. Res.-Atmos. 110.

559 Kim, Y.J., et al., 2014. Modeled aerosol nitrate formation pathways during wintertime in the
560 Great Lakes region of North America. Journal of Geophysical Research: Atmospheres,
561 2014JD022320.
562 Kinne, S., et al., 2006. An AeroCom initial assessment - optical properties in aerosol component
563 modules of global models. Atmos. Chem. Phys. 6, 1815-1834.
564 Lanz, V.A., et al., 2007. Source apportionment of submicron organic aerosols at an urban site by
565 factor analytical modelling of aerosol mass spectra. Atmos. Chem. Phys. 7, 1503-1522.
566 Liu, P.S.K., et al., 2007. Transmission Efficiency of an Aerodynamic Focusing Lens System:
567 Comparison of Model Calculations and Laboratory Measurements for the Aerodyne
568 Aerosol Mass Spectrometer. Aerosol Sci. Technol. 41, 721 - 733.
569 Liu, X., et al., 2012. Toward a minimal representation of aerosols in climate models: description
570 and evaluation in the Community Atmosphere Model CAM5. Geoscientific Model
571 Development 5, 709-739.
572 Malm, W.C., et al., 1994. Spatial and seasonal trends in particle concentration and optical
573 extenction in the United States. J. Geophys. Res.-Atmos. 99, 1347-1370.
574 Mann, G.W., et al., 2014. Intercomparison and evaluation of global aerosol microphysical
575 properties among AeroCom models of a range of complexity. Atmos. Chem. Phys. 14,
576 4679-4713.
577 Middlebrook, A.M., et al., 2012. Evaluation of Composition-Dependent Collection Efficiencies
578 for the Aerodyne Aerosol Mass Spectrometer using Field Data. Aerosol Sci. Technol. 46,
579 258-271.
580 Myhre, G., et al., 2013. Radiative forcing of the direct aerosol effect from AeroCom Phase II
581 simulations. Atmos. Chem. Phys. 13, 1853-1877.
582 Ng, N.L., et al., 2011a. Real-Time Methods for Estimating Organic Component Mass
583 Concentrations from Aerosol Mass Spectrometer Data. Environ. Sci. Technol. 45, 910-
584 916.
585 Ng, N.L., et al., 2010. Organic aerosol components observed in Northern Hemispheric datasets
586 from Aerosol Mass Spectrometry. Atmos. Chem. Phys. 10, 4625-4641.
587 Ng, N.L., et al., 2011b. An Aerosol Chemical Speciation Monitor (ACSM) for Routine
588 Monitoring of the Composition and Mass Concentrations of Ambient Aerosol. Aerosol
589 Sci. Technol. 45, 780-794.
590 Paatero, P., Tapper, U., 1994. Positive matrix factorization - a nonnegative factor model with
591 optimal utilization of error-estimates of data values. Environmetrics 5, 111-126.
592 Perraud, V., et al., 2012. Nonequilibrium atmospheric secondary organic aerosol formation and
593 growth. Proceedings of the National Academy of Sciences 109, 2836-2841.
594 Reid, S.B., et al., 2004. Research and development of planned burning emission inventories for
595 the Central States Regional Air Planning Association. Final Report Prepared for The
596 Central States Air Resource Agencies and The Central Regional Air Planning
597 Association, Oklahoma City, OK.
598 Schneider, J., et al., 2006. Mass spectrometric analysis and aerodynamic properties of various
599 types of combustion-related aerosol particles. Int. J. Mass Spectrom. 258, 37-49.
600 Seinfeld, J.H., Pandis, S.N., 2006. Atmospheric Chemistry and Physics: from air pollution to
601 climate change 2nd ed. John Wiley & Sons, Inc, Hoboken, New Jersey.
602 Sheridan, P.J., et al., 2001. Four years of continuous surface aerosol measurements from the
603 Department of Energy's Atmospheric Radiation Measurement Program Southern Great
604 Plains Cloud and Radiation Testbed site. J. Geophys. Res.-Atmos. 106, 20735-20747.

605 Spracklen, D.V., et al., 2011. Aerosol Mass Spectrometer constraint on the global secondary
606 organic aerosol budget. Atmos. Chem. Phys. 11, 12109-12136.
607 Stokes, G.M., Schwartz, S.E., 1994. The atmospheric radiation - measurement (ARM) program -
608 programmatic background and design of the cloud and radiation test-bed. Bulletin of the
609 American Meteorological Society 75, 1201-1221.
610 Sun, Y., et al., 2012. Characterization of summer organic and inorganic aerosols in Beijing,
611 China with an Aerosol Chemical Speciation Monitor. Atmos. Environ. 51, 250-259.
612 Tiitta, P., et al., 2014. Chemical composition, main sources and temporal variability of PM1
613 aerosols in southern African grassland. Atmos. Chem. Phys. 14, 1909-1927.
614 Tsigaridis, K., et al., 2014. The AeroCom evaluation and intercomparison of organic aerosol in
615 global models. Atmos. Chem. Phys. 14, 10845-10895.
616 Ulbrich, I.M., et al., 2009. Interpretation of organic components from Positive Matrix
617 Factorization of aerosol mass spectrometric data. Atmos. Chem. Phys. 9, 2891-2918.
618 Wexler, A.S., Johnston, M.V., 2008. What have we learned from highly time-resolved
619 measurements during EPA's Supersites program,and related studies? J. Air Waste
620 Manage. Assoc. 58, 303-319.
621 Wiedinmyer, C., et al., 2011. The Fire INventory from NCAR (FINN): a high resolution global
622 model to estimate the emissions from open burning. Geoscientific Model Development 4,
623 625-641.
624 Zhang, Q., et al., 2007a. Ubiquity and dominance of oxygenated species in organic aerosols in
625 anthropogenically-influenced Northern Hemisphere midlatitudes. Geophysical Research
626 Letters 34.
627 Zhang, Q., et al., 2011. Understanding atmospheric organic aerosols via factor analysis of
628 aerosol mass spectrometry: a review. Anal. Bioanal. Chem. 401, 3045-3067.
629 Zhang, Q., et al., 2007b. A Case Study of Urban Particle Acidity and Its Influence on Secondary
630 Organic Aerosol. Environ. Sci. Technol. 41, 3213-3219.
631

Table 1. Summary of the major NR-PM_1 species mass concentrations in units of μg m^{-3} measured at ~ 30 min time resolution over entire study (Nov. 2010 – June 2012) with the average percent of total NR-PM_1 in parentheses.

	$\bar{x}$±1σ	Median	Range	# of Points	DL[b]
Total	7.0±9.3	4.5	0.10 – 270	19148	-
Nitrate	1.5±3.0 (21%)	0.30	BD [a] - 42	19148	0.012
Sulfate	0.80±1.0 (12%)	0.40	BD - 9.6	19148	0.024
Ammonium	0.66±1.2 (9.4%)	0.17	BD - 12	19148	0.284
Chloride	0.020±0.040 (0.24%)	BD	BD – 2.0	19148	0.01
Organics	4.0±6.2 (57%)	2.8	0.10 – 201	19148	0.148
OOA-1	2.1±1.7 (30%)	1.7	BD – 45	19074	-
OOA-2	1.6±2.4 (22%)	0.90	BD – 62	19074	-
BBOA	0.41±3.1 (5.9%)	0	BD – 124	7077	-

[a] Below detection limit (DL). [b]30 minute detection limits in units of μg m^{-3} reported by Ng et al. (2011b). To determine DL for longer averaging times (t) multiply reported DL values by $(t_{30}/t)^{1/2}$.

Figure 1. Plots (a-f) show back trajectories divided by season for 2010-2012 data with the SGP as the end point of each trajectory and are colored by frequency. Note that winter consists of December, January, and February; spring consists of March, April, and May; summer consists of June, July, and August; and fall consists of September, October, and November. Plots (g-h) show the emission rates for CO and isoprene, respectively. All maps have white dots that indicate SGP site location. Maps range from 30 to 50 N and 110 to 80 W.

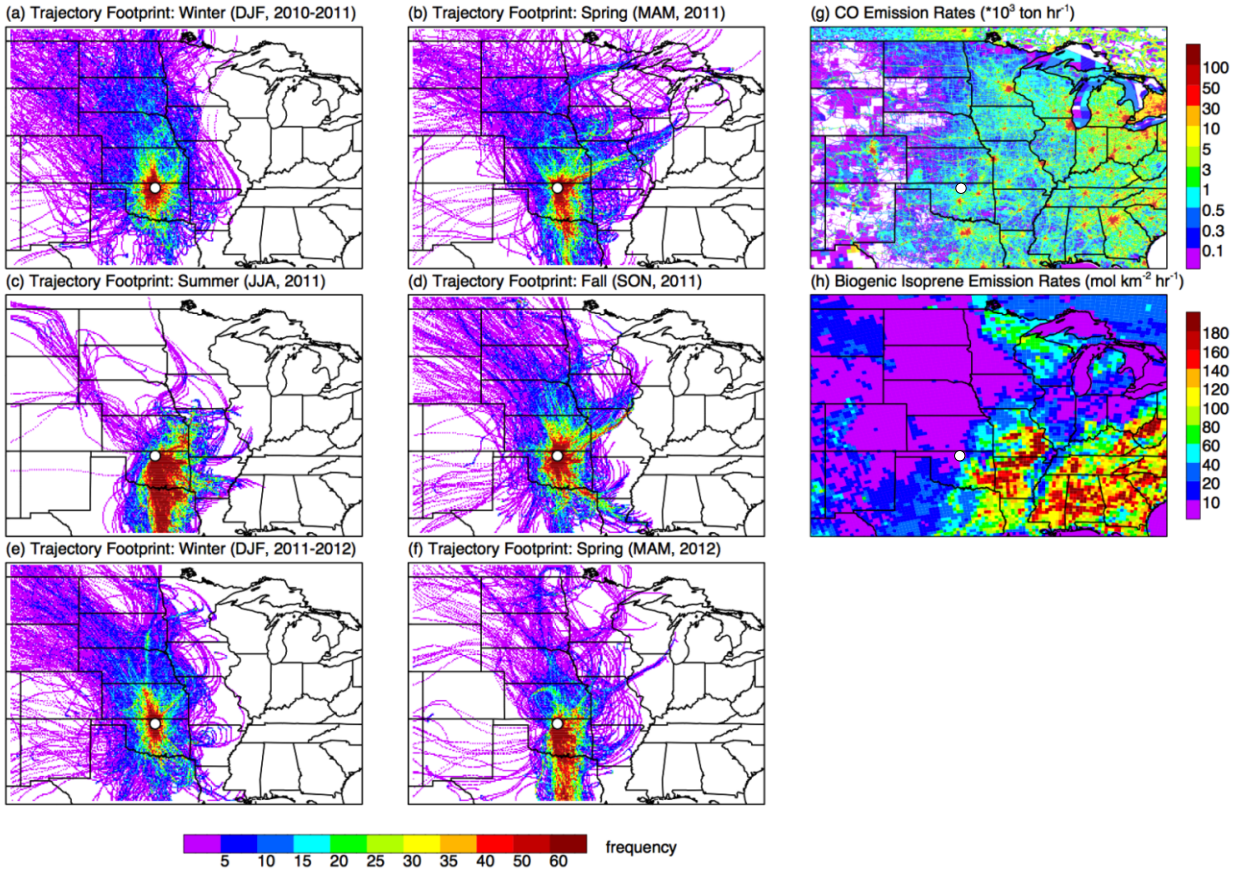

Figure 2. This figure shows the main results from the period 11/20/2010 – 06/28/2012. Shown here are: (a) the daily averaged temperature and relative humidity; (b) the calculated particle density using daily averaged time resolution; (c) the total mass concentration of NR-PM_1 measured by the ACSM in 30 min. (gray) and daily (black) time resolution. (d) and (e) the daily averaged mass concentrations of organic and inorganic species. The gray vertical line that runs through all parts of Figure 2 divides 2011 and 2012 data. Note that y-axes are split in part c and e.

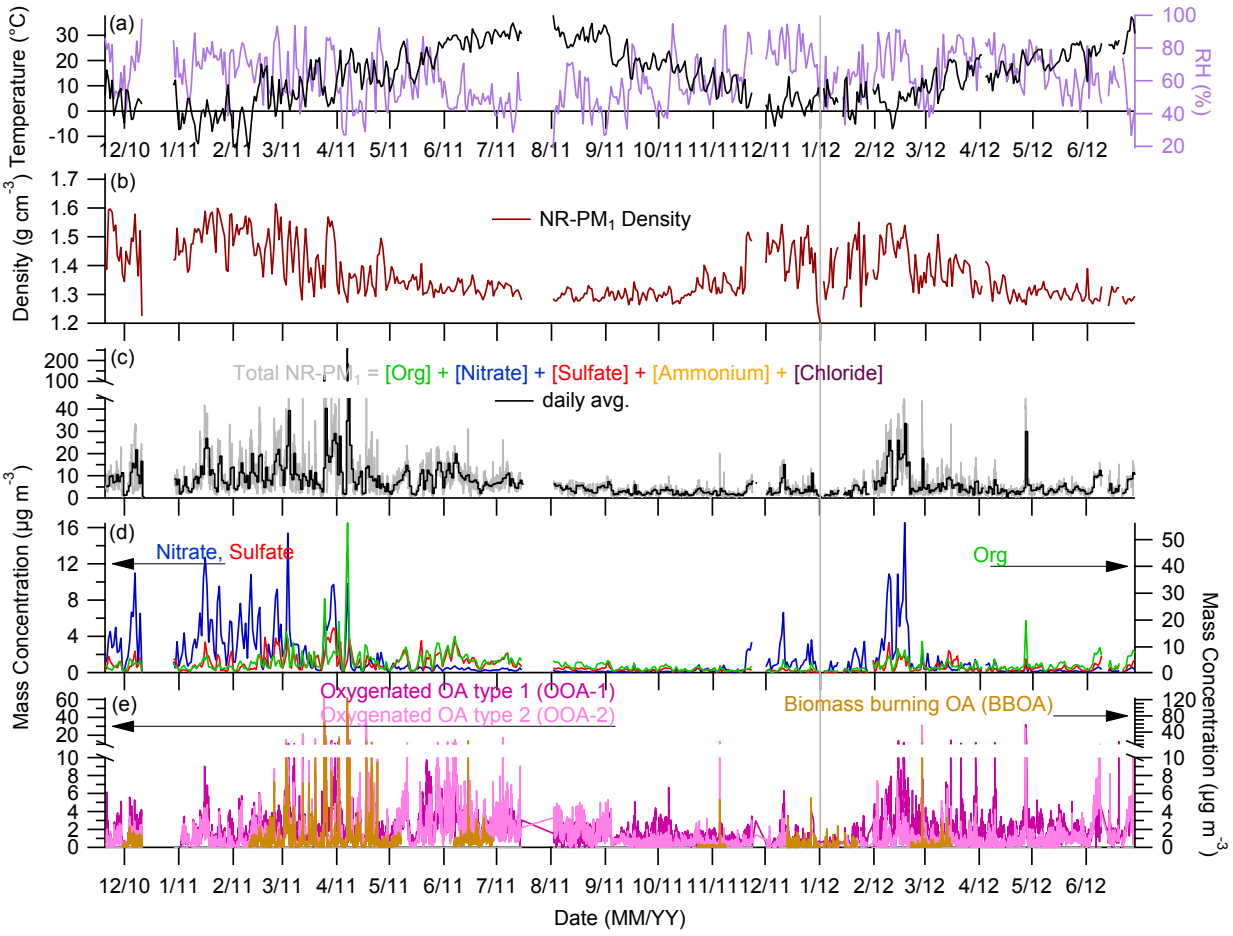

Figure 3. Average mass spectra of three components with standard error bars (a – c). The percentage of the signal above *m/z* 120 is 3.6%, 3.4% and 8.0% for OOA-1, OOA-2 and BBOA, respectively.

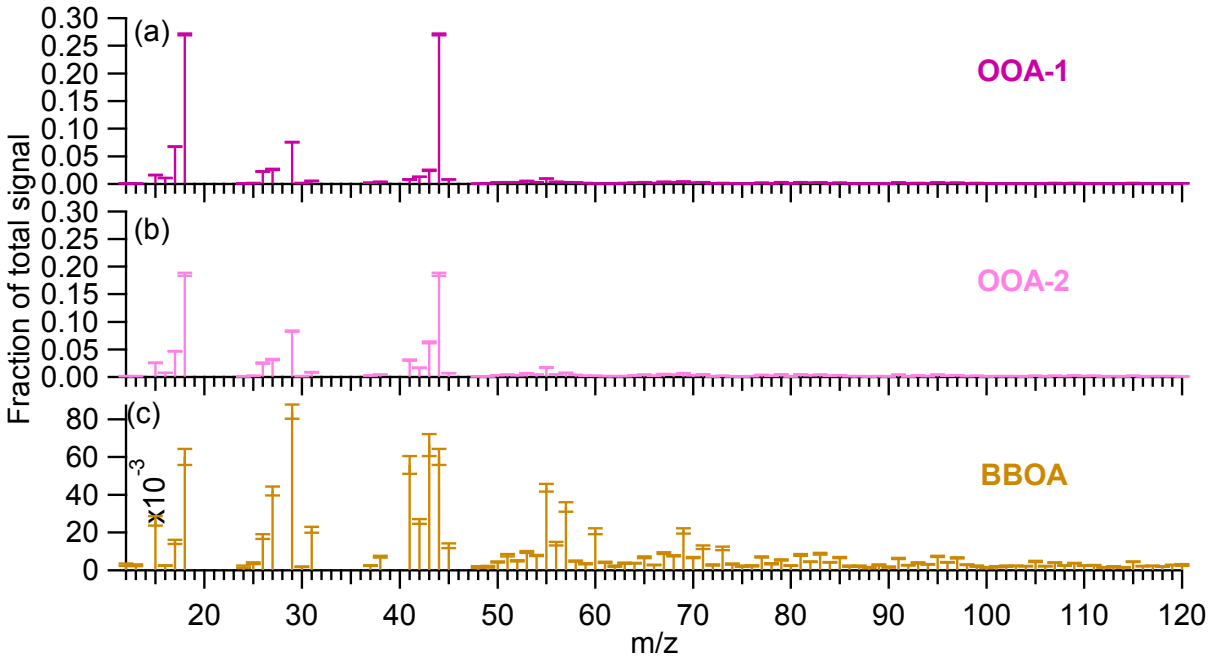

Figure 4. Triangle plot (a) shows the organic f_{43} versus f_{44} for the entire study (open circles) colored by percent of BBOA and sized by total organic mass concentration, using lines provided in referenced paper (Ng et al., 2010). Solid squares represent the mean f_{43} vs f_{44} values for the PMF factors OOA-1, OOA-2 and BBOA. The crosses are the median values and the left and right sides of the box (and bottom and top) are the 25th and 75th percentile, respectively, and the outer whiskers from left to right (and bottom to top) are the 10th and 90th percentile, respectively. Also included are f_{43} and f_{44} values from previous studies, including values for semi-volatile (SV-OOA) and low-volatility oxidized OA (LV-OOA) factors. A similarly formatted graph is shown in part (b) showing organic f_{60} versus f_{44} values. The triangle lines for plot (b) are adapted from Cubison et al. (2011).

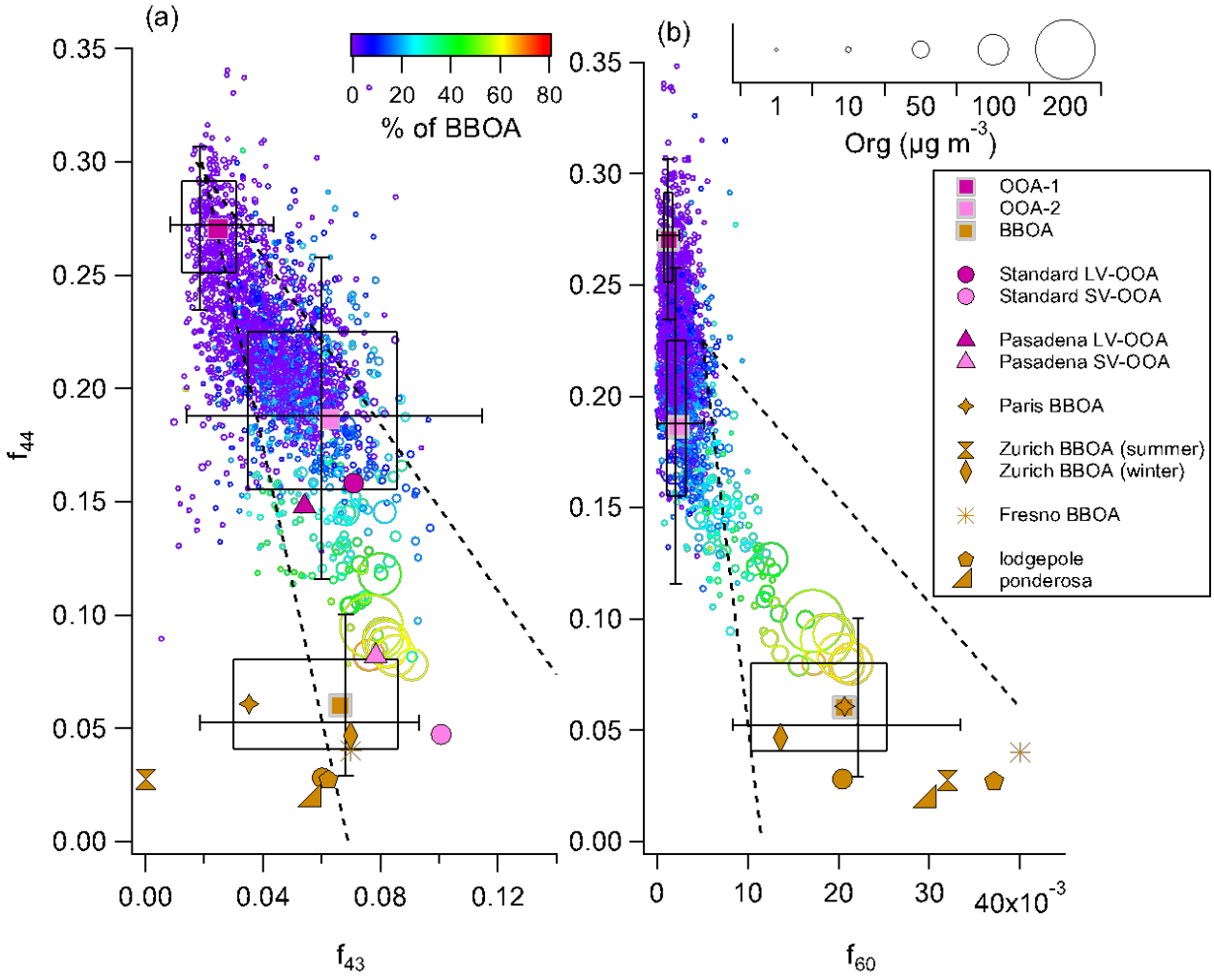

Figure 5. The monthly variations in average NR-PM_1 mass concentration, composition and wind data for one year (Jan. – Dec. 2011). The August wind rose is a reference for all wind roses shown, where the colors of the wind roses correspond to speeds listed in the left box. The middle pie charts show the average composition of organics and have areas that are scaled to total organic loading for that month. The inner pie charts show the average composition of NR-PM_1 and have areas scaled by the average mass loading, written below each month in units of µg m^{-3}, during that month.

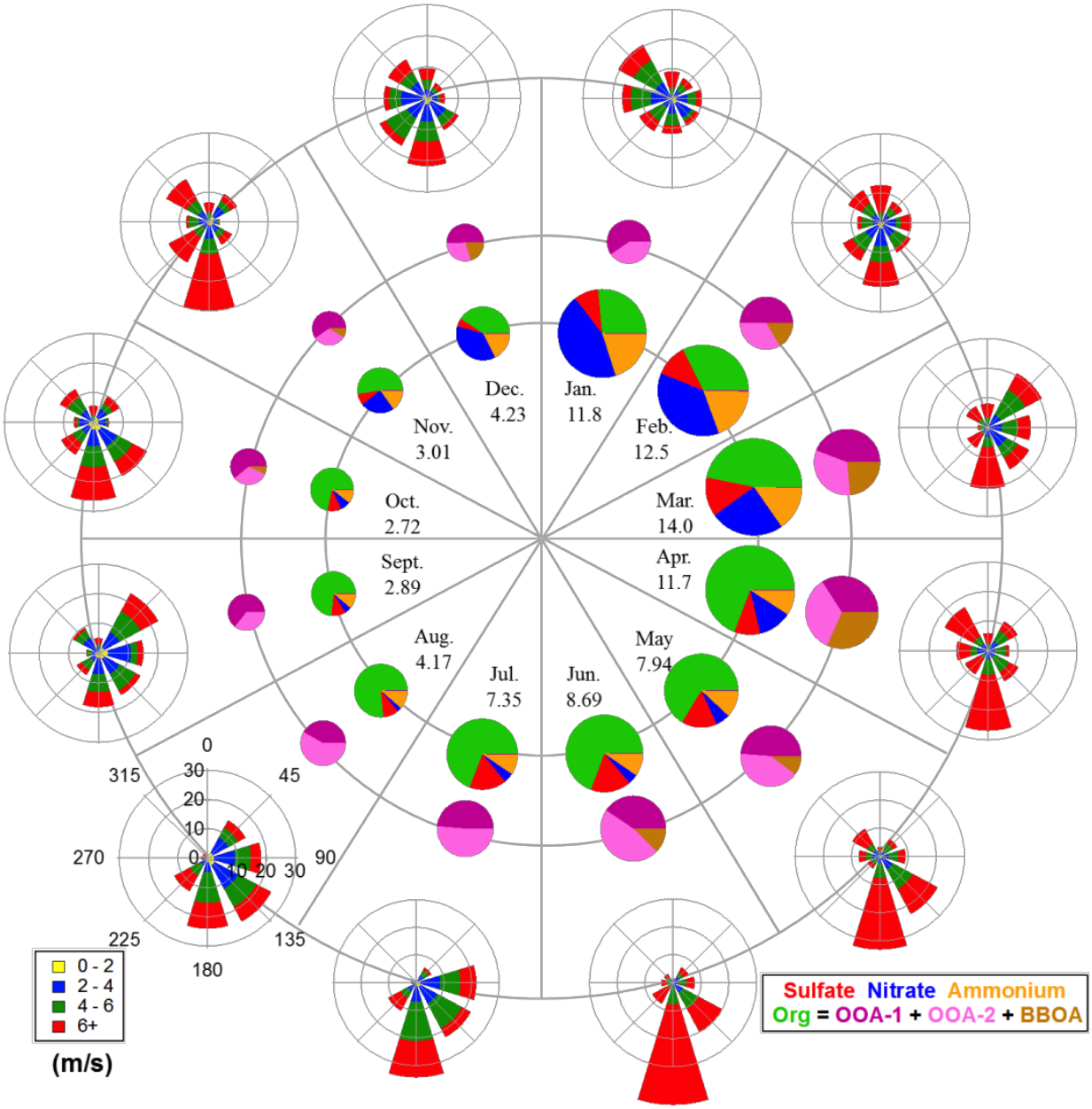

Figure 6. Seasonal characterization of wind and NR-PM_1 composition for 11/20/2010 – 06/28/2012: (a) the averaged wind speed and wind direction for each season, (b) the seasonally averaged mass concentrations of NR-PM_1 species stacked together, and (c) the fractional contribution of each species to total NR-PM_1 mass concentration for each season. The key for the wind roses is shown on the far right wind rose on (a). The total averaged NR-PM_1 mass concentration is displayed above each bar in (b).

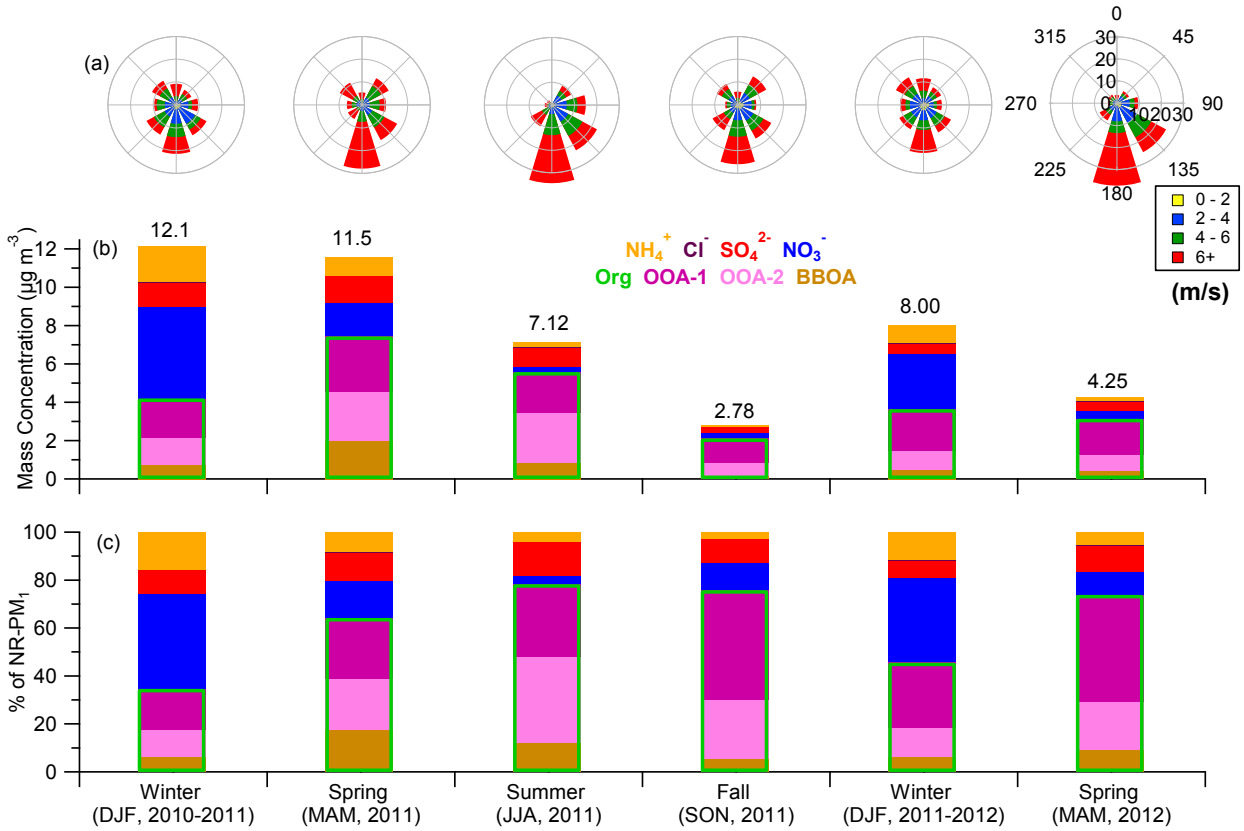

Figure 7. Diurnal variations of temperature, relative humidity (RH), and NR-PM_1 species mass concentrations at SGP for11/20/2010 – 06/28/2012 summarized by season, with mean values shown here. Refer to Figure 1 for seasonal classification.

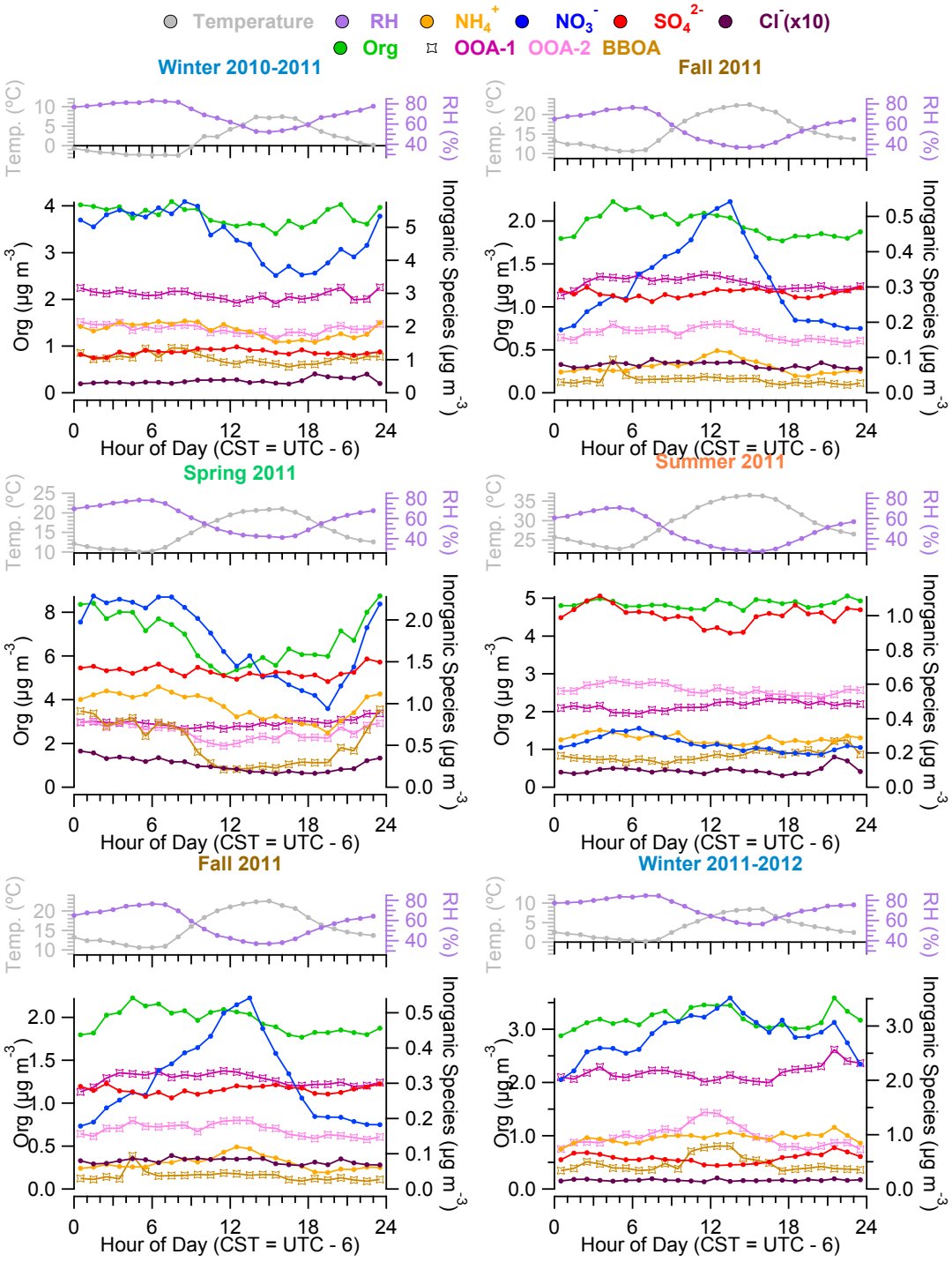

Figure 8. Daily fire emissions of organic carbon for 2011 (a) and March (c) at locations around SGP. The traces are colored according to the boxes highlighted in (e) and (f). Parts (b) and (d) show the daily observation of BBOA concentration at the SGP site for 2011 and specifically for March 2011, respectively. For months with BBOA emissions (March and July 2011) fire locations (e, f) and back trajectories (g, h) are displayed, respectively.

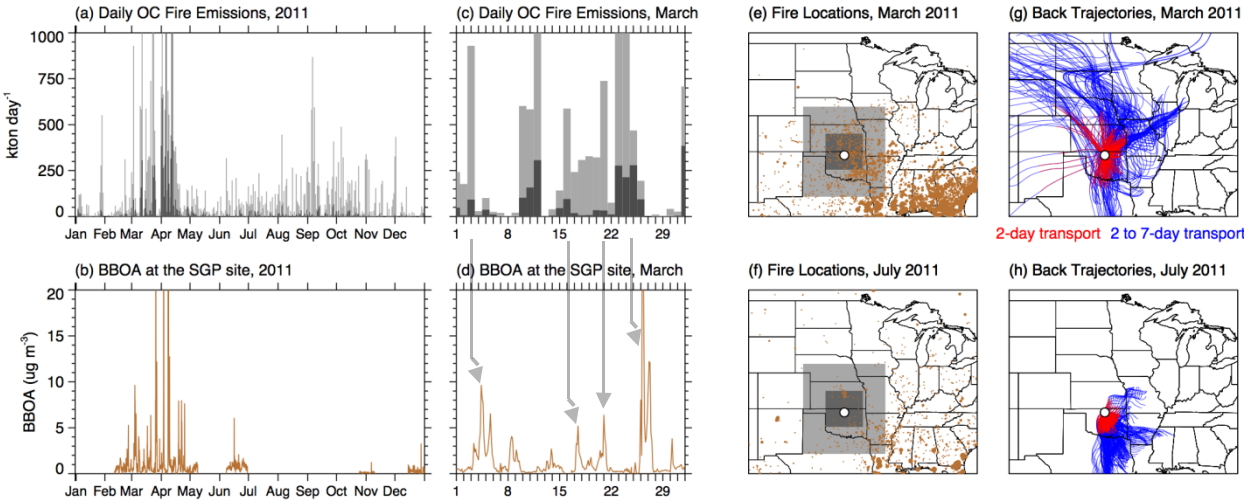

Figure 9. Mass concentration time series for nitrate and ammonium for periods with high mass concentrations are shown in (a). Gray shading represents periods when temperatures at SGP site are below 3°C (dotted line in b). Emission maps for precursor gases including ammonia (c) and NO_x (d) are colored by emission rates. Back trajectories for nitrate including 3-day (red) and 3 to 7-day (blue) transport times to SGP site are shown in (e-h). Similarly formatted time series for sulfate shown in (i) and back trajectories shown in (j – l). Gray dots in (j – l) represent point sources of sulfur dioxide.